Backscattering-Induced Dissipative Solitons in Ring Quantum Cascade Lasers

Lukas Seitner,[1,*] Johannes Popp,[1] Ina Heckelmann,[2] Réka-Eszter Vass,[2,3] Bo Meng,[2,4] Michael Haider,[1] Jérôme Faist,[2] and Christian Jirauschek[1,5,†]

[1]TUM School of Computation, Information and Technology, Technical University of Munich (TUM), 85748 Garching, Germany
[2]Institute for Quantum Electronics, Eidgenössische Technische Hochschule Zürich, 8092 Zurich, Switzerland
[3]Physik-Institut, Universität Zürich, 8057 Zurich, Switzerland
[4]State Key Laboratory of Luminescence and Applications, Changchun Institute of Optics, Fine Mechanics and Physics, Chinese Academy of Sciences, Changchun 130033, People's Republic of China
[5]TUM Center for Quantum Engineering (ZQE), 85748 Garching, Germany

(Received 18 April 2023; revised 25 October 2023; accepted 27 November 2023; published 24 January 2024)

Ring quantum cascade lasers have recently gained considerable attention, showing ultrastable frequency comb and soliton operation, thus opening a way to integrated spectrometers in the midinfrared and terahertz fingerprint regions. Thanks to a self-consistent Maxwell-Bloch model, we demonstrate, in excellent agreement with the experimental data, that a small but finite coupling between the counterpropagating waves arising from distributed backscattering is essential to stabilize the soliton solution.

DOI: 10.1103/PhysRevLett.132.043805

Introduction.—A dissipative soliton is a localized waveform exhibiting the unique property of traveling unperturbed through nonlinear and dispersive media while experiencing gain and loss [1–3]. These structures appear in various optical, but also other physical systems, and there has been growing interest in their occurrence in passive and active microcavities [4–8]. An active microresonator can be realized by a semiconductor gain medium embedded in a ring cavity. Recently, ring quantum cascade lasers (QCLs) received considerable attention, as these devices showed self-starting frequency comb operation with solitonlike spectra [8–11]. The QCL exploits optical intersubband transitions in the conduction band of a multi-quantum-well heterostructure to access large portions of the midinfrared and terahertz regimes [12]. In Fabry-Pérot QCLs, comb generation arises from four-wave-mixing nonlinearities in which dynamical spatial hole burning (SHB) plays a dominant role [13–18]. The Kerr nonlinearity inside a QCL mainly originates from the fast gain saturation, which makes the four-wave mixing very broadband [19]. The absence of SHB for unidirectional propagation in ring QCLs would indicate physics of comb formation that is different from that in Fabry-Pérot resonators [15]. An explanation for multimode operation in ring QCLs was given based on phase turbulence and the linewidth enhancement factor (LEF), where a finite LEF makes gain saturation act as an effective Kerr nonlinearity [10,20]. Injected ring QCLs have been predicted to produce either phase or cavity solitons, dependent on the strength of the injection signal [21]. A generalized form of the Lugiato-Lefever equation can be used to model the system dynamics [22,23]. However, the direct simulation of solitons in free-running ring QCLs with realistic parameters and results as observed in experiment [8] is still missing. Using Maxwell-Bloch theory [24,25], we reveal the physical mechanisms and identify the requirements leading to the recent experimental observation of solitons in free-running ring QCLs. Our approach shows that distributed backscattering in the cavity is necessary for stable soliton solutions, contrasting previous work, which assumed pure unidirectional operation to be favorable [8]. Furthermore, this differs significantly from previous work that introduced just a single or, at most, a few macroscopic cavity interruptions, yielding standing wave patterns [10,26,27]. In our case, considering both propagation directions at once reveals that a fainter counterpropagating wave plays a crucial role in soliton stability. Under these circumstances, a single symmetric Lorentzian gain shape associated with the lasing transition in the Maxwell-Bloch model suffices to obtain the measured system properties. Direct comparison with experiment yields excellent agreement, thus giving valid and novel insights into the dynamics of quantum cascade ring lasers.

Theoretical model.—Our approach to accurately model the dynamics in a ring QCL is based on the one-dimensional multilevel Maxwell-Bloch equations [25,28]. Hence, we simulate the density matrix dynamics and electric field in propagation direction x and time t, with periodic boundary conditions to mimic the ring cavity. To obtain an initial density matrix, the electron transport in the QCL active region is modeled using the ensemble Monte Carlo method [29,30]. A set of eigenstates is obtained by solving the Schrödinger-Poisson equation for seven levels per period, using EZ states as a basis [31]. The obtained gain of the structure, as used in [8], exhibits an unsaturated value of $g_0 = 16.5\ \mathrm{cm}^{-1}$ at the

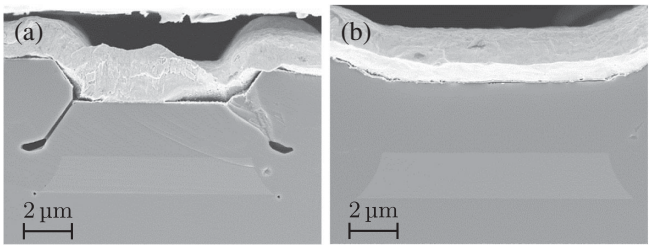

FIG. 1. Images of cleaved waveguide cross sections obtained using a scanning electron microscope. (a) Device with defects and thus increased backscattering. (b) Defect-free device from another fabrication run.

center frequency $f_c = 40.89$ THz (see Sec. I.A. of the Supplemental Material [32] for more details). The time evolution of the density matrix, describing the state of the multilevel quantum system, is governed by the Liouville–von Neumann master equation, using the rotating wave approximation [25]. The closed set of equations used for the time evolution of the density matrix can be found in detail in [33]. The electric field amplitude in the slowly varying amplitude approximation is described as the superposition of a left- and right-traveling wave. For both components $E^{\pm}$, a classical propagation equation can be derived from Maxwell's equations, given by

$$\partial_t E^{\pm} = \mp v_g \partial_x E^{\pm} + f^{\pm}(x,t) - lE^{\pm} - \mathrm{i} v_g \frac{\beta_2}{2} \partial_t^2 E^{\pm}. \quad (1)$$

In Eq. (1), we consider losses l, the group velocity v_g, as well as the background group velocity dispersion (GVD) β_2 of the effective material, as they have a non-negligible influence on frequency comb formation [36]. The second term $f^{\pm}(x,t)$ in (1) refers to the polarization originating from the quantum system. An explicit expression for $f^{\pm}(x,t)$ is derived from the density matrix equations in Sec. I.C. of the Supplemental Material [32].

In ring lasers, the counterpropagating wave components E^+ and E^- are commonly referred to as clockwise (CW) and counterclockwise (CCW) fields. In Eq. (1), E^+ and E^- are not coupled directly but may only interact via the density matrix. As in ring lasers, cross-gain saturation exceeds self-gain saturation, a spontaneous symmetry breaking between the two counterpropagating fields will occur for large enough pumping [34,35]. In real devices, considerable backscattering may occur due to fabrication defects, introducing a finite optical coupling between these fields, even after symmetry breaking. The central message of this Letter is that this coupling between the counterpropagating modes in the free-running ring cavity is an essential element for soliton formation and stability. In Fig. 1, two cleaved cross sections of waveguides from the same wafer but from different fabrication runs are exemplarily shown, captured by a scanning electron microscope. In Fig. 1(a), a device clearly exhibiting microscopic defects surrounding the active region is depicted. Since the electromagnetic field overlaps with these defects, it experiences an impedance mismatch, leading to localized reflections. As we assume the presence of many such defects throughout the cavity, this effect sums up to significant backscattering. A device from the same fabrication run, therefore having comparable backscattering, clearly showed soliton operation [8]. In Fig. 1(b), a cross section of a defect-free cavity from another fabrication run is presented for comparison. In similar devices, only minimal backscattering is present, and pure single-mode operation was experimentally observed in free-running operation.

Our model simultaneously considers both propagation directions (CW and CCW) and couples them through backscattering. The microscopic defects are introduced by subdividing the cavity into numerous regions with a small field reflection coefficient r defined as $\Delta E^{\pm} = rE^{\mp}$, at each interface, where $\Delta E^{\pm}$ denotes the resulting field change. Thus, both field components experience the same relative amount of reflection and compete for the available gain, leading to a strongly nonlinear relation between r and the power in the reflected wave. Therefore, a sufficient number of scatterers with small reflections is essential, such that both field directions remain traveling waves (see also Supplemental Material [32] Sec. I.B).

Results.—As cavity losses typically exceed backscattering by orders of magnitude, the field backscattering coefficient α can hardly be retrieved by reflection measurements. Therefore, α is estimated by the ratio of the symmetry-breaking current I_{sym} to the threshold current I_{th} [34,37]. The Maxwell-Bloch equations inherently capture the full dynamics when varying the pump current and simulating both propagation directions. In order to extract α, we perform a current sweep, locate the symmetry-breaking point, and compare the results to measured light-current (LI) curves. Assuming a mainly photon-driven current, a full sweep can be approximated by varying the dipole moment μ accounting for the band-edge tilting, and the resulting change in the wave function overlap with increasing bias [38]. The measured and simulated LI curves are shown in Fig. 2 and yield $\alpha \approx 0.01$ cm^{-1} for Fig. 2(a) an imperfect cavity and $\alpha \approx 0.0001$ cm^{-1} for Fig. 2(b) a defect-free cavity (for comparison, the field losses are $\approx$1.5 cm^{-1}). Using 100 regions with $r = 0.0008$ in Fig. 2(a) and $r = 0.0001$ in Fig. 2(b) at each interface, we obtain very good agreement of the intracavity power and the ratio $I_{\mathrm{sym}}/I_{\mathrm{th}}$. The slight remaining difference can be mainly attributed to the fact that only photon-driven current is varied in the simulation. Additionally, the experimental setup will always have incomplete mode contrast, as reflections of the field in the main propagation direction on the InP-air interfaces can be captured. This may lead to an overestimation of the actual intracavity intensity of the counterpropagating mode in the measurement.

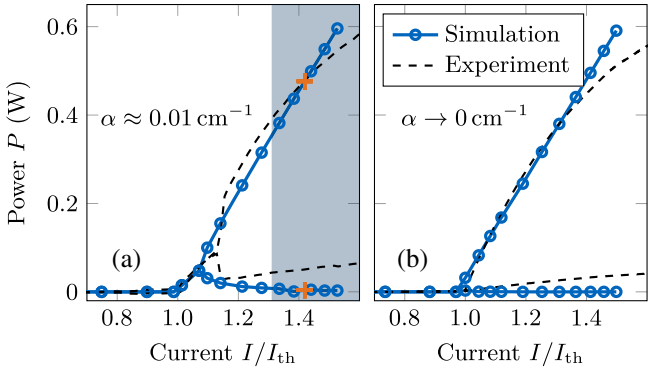

FIG. 2. Simulated and experimental intracavity power versus normalized bias current. In (a) significant and in (b) negligible backscattering α is present. The shaded area in (a) marks the multimode regime observed in simulations. The orange crosses mark the bias used for dynamical simulations.

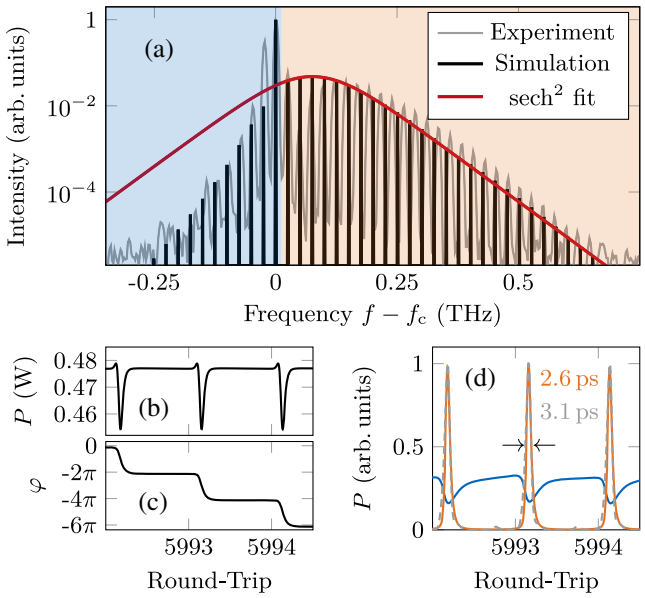

FIG. 3. (a) Intensity spectra of simulation and experiment showing a soliton shape. (b) Simulated intracavity power (P) of the main propagation direction showing the propagating soliton. (c) Corresponding phase (φ) profile. (d) Filtered intensity contributions of the time trace in (b), with the normalized measured and filtered pulses from dual-comb spectroscopy (gray dashed) shown for comparison.

When a certain amount of backscattering is present, as shown in Fig. 2(a), multimode operation can be sustained in a steady state, and soliton generation is possible. This bias region is shaded in blue (gray) color for the simulation. Different multimode operation regimes besides single soliton operation, such as double pulsing and more irregular comb shapes, are observed, in agreement with experimental observations [8] (see Figs. 4 and 5 of the Supplemental Material [32]). When decreasing the reflection value, the onset of stable multimode operation gets shifted to higher bias currents. Choosing $r = 0.0001$, as in Fig. 2(b), only single-mode spectra were obtained in the considered bias region, as also confirmed by experiment. Therefore, with a reflection of $r = 0$, multimode operation will be stable only at the Risken-Nummedal-Graham-Haken (RNGH) instability bias, which is 9 times the lasing threshold [39,40]. This instability bias is lowered by interference between counterpropagating fields [13] arising here due to defect-induced backscattering. It thus opens up the possibility of multimode operation in a reasonable bias range of ring QCLs. At the bias point considered for the long-term simulation [orange cross in Fig. 2(a), results of Fig. 3], the minimum reflection for stable soliton operation was found to be $r \approx 0.0006$, i.e., slightly below the value of Fig. 2(a). Furthermore, the defect-free device of Fig. 2(b) is for realistic biases clearly below the multimode threshold. A larger value of α, i.e., increased backscattering, would bring the multimode bias closer to the lasing threshold, until standing wave dynamics become dominant. For further analysis, we choose the point marked with the orange cross in Fig. 2(a), as this point contains the extracted dipole element at the bias voltage where the self-consistent Monte Carlo simulation has been performed.

We simulate over 6000 round-trips, of which the last 2000 are postprocessed as a steady-state solution. The overall intracavity power of roughly 480 mW fits well with the one of the experimental device in [8]. Applying a Fourier transform to the converged field yields the spectrum shown in Fig. 3(a). The characteristic sech-square shape of soliton operation can be observed in the spectral range above the center frequency. This envelope very well describes 25 of the comb teeth, which is in near-perfect agreement with the experimental results. The individual comb lines do not show an intermodal phase difference, which suggests that they are phase locked, except for the center mode, which is shifted by π (see Sec. II.A. of the Supplemental Material [32]). The comb exhibits a clear beat note at roughly 25 GHz. The linewidth is below our numerical frequency resolution of ≈5 MHz. The inclusion of spontaneous emission noise [41] does not significantly influence the spectral phase relations and the beat note linewidth. Unprocessed temporal results of the last three round-trips are shown in Fig. 3(b) and reveal an amplitude modulation in the form of an intensity dip. The corresponding temporal phase shown in Fig. 3(c) exhibits a 2π jump at each amplitude dip, bearing remarkable similarity to the injected phase soliton predicted in [21]. Thus, the counterpropagating field might be interpreted as a weak self-injecting signal. The intensity features a strong continuous wave background, but various applications of optics are based on short, background-free pulses. A reliable generation of such in the midinfrared region holds large technological potential. As only one side of the spectrum follows the characteristic sech-square shape of a Kerr-type soliton, the authors of [8] applied an optical

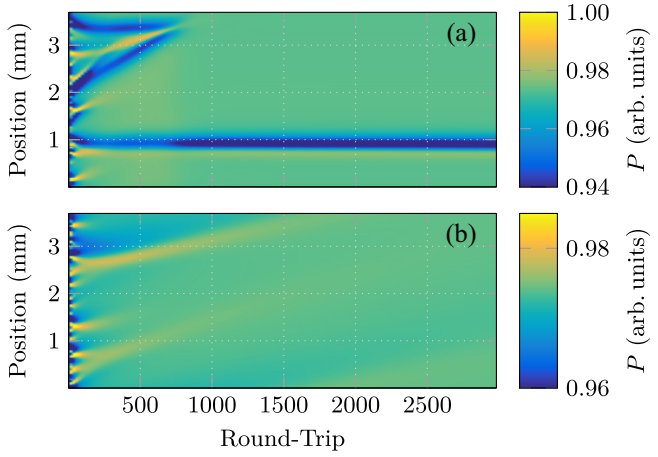

FIG. 4. Intracavity power distribution in main propagation direction for 3000 round-trips. (a) With backscattering, clear localized structures emerge and remain stable unless they collide. (b) Without backscattering, weakly modulated localized structures may form but eventually fade out.

filter to isolate single pulses. Accordingly, we filter the simulated spectrum, such that the blue (dark gray) shaded part of Fig. 3(a) contains field components with frequencies $f \leq f_c$ and the orange-shaded (light gray) part contains the contributions with $f > f_c$. Separately transforming each filtered comb part to the time domain yields two intensity contributions plotted in blue (dark gray) and orange (light gray) colors, respectively, in Fig. 3(d). The filtered intensities show a pulsed waveform superimposed to a dispersive continuous background wave, in complete agreement with the experiment. The pulse width is 2.6 ps, which is very close to the measured value of 3.1 ps.

An intuitive understanding of the physical mechanisms that enable soliton generation and stabilization can be obtained by investigating the spatiotemporal evolution of the optical power in the cavity, as depicted in Fig. 4 for the main propagation direction. In Fig. 4(a), sufficient backscattering is included to be above the multimode stability threshold [as in Figs. 1(a) and 2(a)], while Fig. 4(b) shows a "clean" cavity below the backscattering threshold [as in Figs. 1(b) and 2(b)]. In both cases, the dynamics of the first ≈100 round-trips are nearly identical. The optical field builds up from random, rapidly oscillating fluctuations. These fluctuations experience gain with limited bandwidth, leading to their decay or a fusion into localized field structures. In Fig. 4(a), several localized structures have formed at around 250 round-trips. Two of them cancel out after around 750 round-trips where only a single localized structure remains, traveling as a stable soliton. Its velocity slightly deviates from the exact speed of light in the cavity, as for the injected phase soliton [21], but we corrected this offset for better visibility. The spatiotemporal evolution of the counterpropagating field does not show significant intensity modulations and can be found in Fig. 8 of the Supplemental Material [32]. In Fig. 4(b), localized field structures form in the first few 100 round-trips, but the modulation eventually fades out due to insufficient stabilization by a counterpropagating wave. The spectrum shows a solitonlike shape in the beginning, similar to combs induced by phase turbulence [10]. But as the temporal amplitude modulation continuously decreases, side modes disappear, resulting in single-mode operation. This finding is experimentally confirmed, as free-running ring QCLs with vanishing backscattering only sustain single-mode operation in steady state for all realized devices.

Discussion.—As described above, adding the distributed backscattering allows the CCW and CW components to interact and stabilize the soliton. In order to identify the mechanisms that lead to the generation of a soliton and its preservation, we shall discuss a further feature of our detailed model. Unlike in other models for ring QCLs, optical interference effects, like SHB, are present from the beginning of the simulation. During the field formation process, when symmetry breaking has not yet occurred, CCW and CW components carry similar amounts of energy (first approximately ten round-trips). Setting the population grating terms in the density matrix equation to zero enforces the absence of SHB. For this case, in the presence of backscattering, both field components stay equally active over the whole simulation time. Consequently, the terms associated with SHB significantly contribute to cross-gain saturation, such that symmetry breaking occurs despite the presence of backscattering, which favors bidirectional operation. Therefore, we conclude that optical interference effects are crucial in the field formation dynamics of free-running ring QCLs. But also in steady state, the interaction between the asymmetric CW and CCW waves provides a whiff of SHB, which triggers multimode operation and lowers the threshold for the RNGH instability [13]. Thus, the main advantage of the ring configuration over Fabry-Pérot cavities is that the amount of backscattering, and hence SHB, can be adjusted. This is especially important in the context of soliton operation since, besides its beneficial effect on multimode operation, excessive SHB induces undesired phase and amplitude instabilities [17].

Frequency combs in free-running ring QCLs are dominated by the phase dynamics and linked to the balance of a Kerr-type nonlinearity with GVD [10]. Both parameters are typically assumed to be constant, and stable multimode operation is obtained when they are correctly balanced, even though only considering one propagation direction. Our model intrinsically features these quantities as frequency- and intensity-dependent values [25] and yields the characteristic phase turbulence during the field formation, even without backscattering. However, the consequent and repeatable vanishing of solitonic modulations that we observe in unidirectional, free-running ring QCLs has not been discussed so far, to the best of our knowledge.

The complete density matrix equations used here fully capture the tendency of QCLs to operate in single mode. This effect dominates over the fragile multimode balance generated by the interplay of nonlinearity and dispersion and forces phase and amplitude modulations to diminish. If, however, sufficient backscattering is present, the counterpropagating field may stabilize the balance. It appears to serve as a source of near-resonant injection, similar to the results of weak external injection forming phase solitons in [21]. Together with the weakly generated SHB, such a self-feeding and phase referencing mechanism for the off-resonant modes may suffice to overcome the single-mode tendency. Thus, the backscattering is the crucial ingredient to sustain the self-generated soliton of the ring QCL.

Conclusion.—We have shown that the occurrence of distributed backscattering can explain the experimental observation of solitons in an active ring cavity. The symmetry breaking between both propagation directions can be captured by sweeping the photon-driven current in the Maxwell-Bloch simulations. The self-consistently calculated seven-level system yields solitons that agree very well with experiment regarding power, bandwidth, and duration. By measurement and simulation, we have shown that a fainter counterpropagating field induced by backscattering enables the formation of a stable localized field structure corresponding to a self-injected phase soliton. These results may open the way to reliable soliton generation in ring QCLs by custom-tailored cavity defects.

*lukas.seitner@tum.de
†jirauschek@tum.de

[1] *Dissipative Solitons*, edited by N. Akhmediev and A. Ankiewicz (Springer, New York, 2005).
[2] P. Grelu and N. Akhmediev, Nat. Photonics **6**, 84 (2012).
[3] T. J. Kippenberg, A. L. Gaeta, M. Lipson, and M. L. Gorodetsky, Science **361**, eaan8083 (2018).
[4] Y. S. Kivshar and G. Agrawal, *Optical Solitons: From Fibers to Photonic Crystals* (Academic Press, San Diego, 2003).
[5] F. Leo, S. Coen, P. Kockaert, S.-P. Gorza, P. Emplit, and M. Haelterman, Nat. Photonics **4**, 471 (2010).
[6] T. Herr, V. Brasch, J. D. Jost, C. Y. Wang, N. M. Kondratiev, M. L. Gorodetsky, and T. J. Kippenberg, Nat. Photonics **8**, 145 (2014).
[7] A. B. Matsko, A. A. Savchenkov, W. Liang, V. S. Ilchenko, D. Seidel, and L. Maleki, Opt. Lett. **36**, 2845 (2011).
[8] B. Meng, M. Singleton, J. Hillbrand, M. Franckié, M. Beck, and J. Faist, Nat. Photonics **16**, 142 (2022).
[9] B. Meng, M. Singleton, M. Shahmohammadi, F. Kapsalidis, R. Wang, M. Beck, and J. Faist, Optica **7**, 162 (2020).
[10] M. Piccardo, B. Schwarz, D. Kazakov, M. Beiser, N. Opačak, Y. Wang, S. Jha, J. Hillbrand, M. Tamagnone, W. T. Chen, A. Y. Zhu, L. L. Columbo, A. Belyanin, and F. Capasso, Nature (London) **582**, 360 (2020).
[11] P. Micheletti, U. Senica, A. Forrer, S. Cibella, G. Torrioli, M. Frankié, M. Beck, J. Faist, and G. Scalari, Sci. Adv. **9**, eadf9426 (2023).
[12] J. Faist, F. Capasso, D. L. Sivco, C. Sirtori, A. L. Hutchinson, and A. Y. Cho, Science **264**, 553 (1994).
[13] C. Y. Wang, L. Diehl, A. Gordon, C. Jirauschek, F. X. Kärtner, A. Belyanin, D. Bour, S. Corzine, G. Höfler, M. Troccoli, J. Faist, and F. Capasso, Phys. Rev. A **75**, 031802(R) (2007).
[14] A. Gordon, C. Y. Wang, L. Diehl, F. X. Kärtner, A. Belyanin, D. Bour, S. Corzine, G. Höfler, H. C. Liu, H. Schneider, T. Maier, M. Troccoli, J. Faist, and F. Capasso, Phys. Rev. A **77**, 053804 (2008).
[15] A. Hugi, G. Villares, S. Blaser, H. C. Liu, and J. Faist, Nature (London) **492**, 229 (2012).
[16] J. B. Khurgin, Y. Dikmelik, A. Hugi, and J. Faist, Appl. Phys. Lett. **104**, 081118 (2014).
[17] P. Tzenov, D. Burghoff, Q. Hu, and C. Jirauschek, IEEE Trans. Terahertz Sci. Technol. **7**, 351 (2017).
[18] D. Burghoff, Optica **7**, 1781 (2020).
[19] P. Friedli, H. Sigg, B. Hinkov, A. Hugi, S. Riedi, M. Beck, and J. Faist, Appl. Phys. Lett. **102**, 222104 (2013).
[20] N. Opačak, S. D. Cin, J. Hillbrand, and B. Schwarz, Phys. Rev. Lett. **127**, 093902 (2021).
[21] F. Prati, M. Brambilla, M. Piccardo, L. L. Columbo, C. Silvestri, M. Gioannini, A. Gatti, L. A. Lugiato, and F. Capasso, Nanophotonics **10**, 195 (2020).
[22] L. A. Lugiato and R. Lefever, Phys. Rev. Lett. **58**, 2209 (1987).
[23] L. Columbo, M. Piccardo, F. Prati, L. A. Lugiato, M. Brambilla, A. Gatti, C. Silvestri, M. Gioannini, N. Opačak, B. Schwarz, and F. Capasso, Phys. Rev. Lett. **126**, 173903 (2021).
[24] L. Allen and J. H. Eberly, *Optical Resonance and Two-Level Atoms* (Dover Publications, New York, 1987).
[25] C. Jirauschek, M. Riesch, and P. Tzenov, Adv. Theory Simul. **2**, 1900018 (2019).
[26] M. Jaidl, N. Opačak, M. A. Kainz, S. Schönhuber, D. Theiner, B. Limbacher, M. Beiser, M. Giparakis, A. M. Andrews, G. Strasser, B. Schwarz, J. Darmo, and K. Unterrainer, Optica **8**, 780 (2021).
[27] D. Kazakov, N. Opačak, M. Beiser, A. Belyanin, B. Schwarz, M. Piccardo, and F. Capasso, Optica **8**, 1277 (2021).
[28] C. Jirauschek and P. Tzenov, Opt. Quantum Electron. **49**, 414 (2017).
[29] C. Jirauschek and T. Kubis, Appl. Phys. Rev. **1**, 011307 (2014).
[30] C. Jirauschek, J. Appl. Phys. **122**, 133105 (2017).
[31] V. Rindert, E. Önder, and A. Wacker, Phys. Rev. Appl. **18**, L041001 (2022).
[32] See Supplemental Material at http://link.aps.org/supplemental/10.1103/PhysRevLett.132.043805 for more details on the active region design, the cavity model, the generalized Maxwell-Bloch equation system, and additional modeling results, which includes Refs. [8,24,25,28,30,33–35].
[33] C. Jirauschek, Laser Photonics Rev. **17**, 2300461 (2023).
[34] M. Sorel, G. Giuliani, A. Scire, R. Miglierina, S. Donati, and P. Laybourn, IEEE J. Quantum Electron. **39**, 1187 (2003).

[35] R. J. C. Spreeuw, R. C. Neelen, N. J. van Druten, E. R. Eliel, and J. P. Woerdman, Phys. Rev. A **42**, 4315 (1990).
[36] D. Burghoff, T.-Y. Kao, N. Han, C. W. I. Chan, X. Cai, Y. Yang, D. J. Hayton, J.-R. Gao, J. L. Reno, and Q. Hu, Nat. Photonics **8**, 462 (2014).
[37] E. J. D'Angelo, E. Izaguirre, G. B. Mindlin, G. Huyet, L. Gil, and J. R. Tredicce, Phys. Rev. Lett. **68**, 3702 (1992).
[38] J. Faist, F. Capasso, C. Sirtori, D. L. Sivco, A. L. Hutchinson, and A. Y. Cho, Nature (London) **387**, 777 (1997).
[39] H. Risken and K. Nummedal, J. Appl. Phys. **39**, 4662 (1968).
[40] R. Graham and H. Haken, Z. Phys. **213**, 420 (1968).
[41] L. L. Columbo, P. Bardella, and M. Gioannini, Opt. Express **26**, 19044 (2018).